Comparative analysis of the Performances and reliability of a Switching Power Amplifier (SPA) for Active Magnetic Bearing Systems: SiC MOSFET Vs Si IGBT Version

André De Andrade [a], Lakdar Sadi-Haddad [a], Ramdane Lateb [a], Joaquim Da Silva [a]

[a] *SKF Magnetic Mechatronics, 2 rue des champs, 27950 Saint Marcel, France*

Abstract

This paper explores the potential advantages of using wide bandgap (WBG) semiconductors, specifically Silicon-Carbide (SiC), over traditional Silicon (Si) in power electronic systems. The authors present a comprehensive comparison between the SiC MOSFET switching power amplifier (SPA) and the Si IGBT SPA, assessing their efficiency, weight, and footprint, as well as the behavior of the SiC SPA in presence of long power cables. Additionally, the durability and reliability of the SiC SPA are analyzed through environmental aging tests such as thermal cycling, vibration, shock tests, and EMC tests. The results show that the SiC SPA is a promising technology with significant advantages over traditional Si SPAs, such as reduced losses, increased efficiency, and decreased weight. However, further qualification tests are needed to ensure its reliability and durability under more demanding conditions. The SiC SPA has the potential to become a valuable solution for a wide range of applications, including oil and gas platforms and sub-marine applications.

Keywords: *Silicon Carbide, Switching Power Amplifier, Power density, Active Magnetic Bearing, efficiency, carbon footprint*

1. Introduction

Wide bandgap (WBG) semi-conductors, such as Silicon-Carbide (SiC), are widely recognized in power electronic circles for their significant advantages over traditional Silicon (Si), such as high-power density, lower losses, and smaller carbon footprint due to their lower energy consumption during operation [1]-[3]. This make them an attractive option for applications where energy efficiency and environmental impact are a concern. Nevertheless, the substantial cost of SiC components remains a major hurdle for their broader implementation in non-embedded industrial applications [4], and despite recent progress in wafer manufacturing [5]-[6].

SiC components were first used in IT infrastructures, renewables, and telecommunication. In automotive application, SiC MOSFET device was applied first by Tesla and followed by others especially in Asia [7]. Some comparative studies between Si IGBT and SiC MOSFET, analyzing three phase inverters [8]-[9] or a power factor controller [10], have shown a significant improvement in efficiency, weight, and size even by increasing the switching frequency. Additional benefits have been highlighted as well, such as a reduction of the heat sink, the output filter with a conclusion of a better cost-effective solution [8]-[9]. Despite the interest in the more electrical aircraft development [11], SiC semi-conductors have limited track record in high reliability applications.

Efforts have been made to comprehensively address the reliability aspects of WBG power devices, which warrant careful consideration [12]. Reliability studies have shown a time drift of the threshold voltage, gate oxide reliability concern and some short-circuit failures [13]-[17], attributed to the relative novelty of the product [18]-[19]. Besides the component itself, its operation within the circuit and the system is equally of importance.

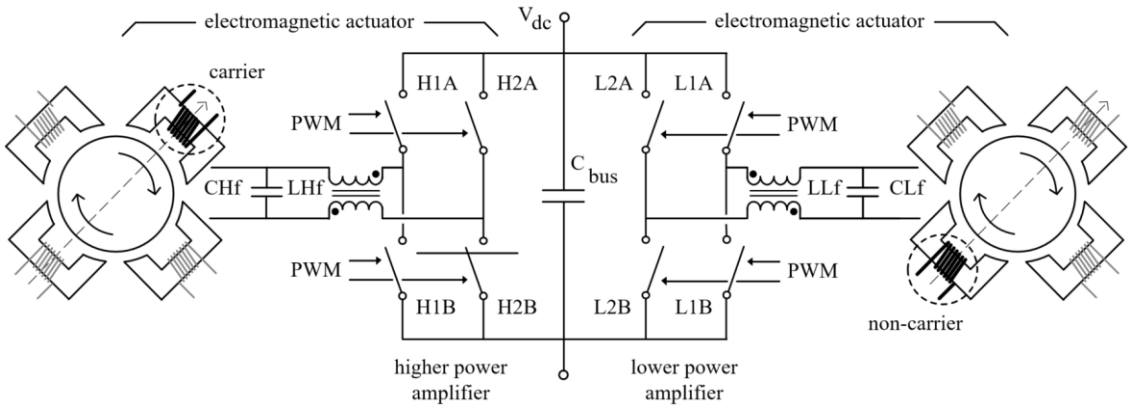

Figure 1 One axis electromagnetic actuator.

A higher dv/dt of SiC MOSFET can increase ringing and adversely affect the EMC/EMI performance, and higher switching frequency causes increased level of common-mode voltage leading to leakage/stray currents such as electric discharge machining type current and capacitive type current [20].

Controllable dv/dt and di/dt behavior of SiC MOSFET has been studied for telecom applications [21], for DC/DC boost converters [22] and for a three-phase inverter using long cables [23]. The use of SiC also holds potential value in the Oil & Gas industry, particularly in applications involving active magnetic bearings controlled by switching power amplifiers (SPA), such as compressors and turbo-expanders. SiC's benefits make it an attractive choice for embedded applications, such as platforms, floating production, storage, and offloading vessels (FPSO), floating storage and offloading units (FSU), and sub-marine applications requiring reliable operation at significant depths. The paper aims to present a comprehensive comparison between two power electronic systems: the SiC MOSFET SPA and the Si IGBT SPA supplying active magnetic bearings (AMBs).

Figure 1 shows a typical representation of two SPA bridges supplying one axis electromagnetic actuator. To achieve this, the authors will assess their efficiency (i.e., losses), weight, and footprint. Additionally, they will investigate the behavior of the SiC SPA in presence of long power cables.

Furthermore, the authors analyze the durability and reliability of the SiC SPA by subjecting it to various environmental aging tests such as thermal cycling, vibration, shock tests, and EMC tests. Through these tests, the authors aim to provide a better understanding of the SiC SPA's performance in real-world conditions.

2. Switching Power Amplifier

2.1. Half bridge Vs full bridge power amplifier

The asymmetric half-bridge (Figure 2) converter is widely recognized as the most used topology in Active Magnetic Bearings (AMBs) due to its simplicity of implementation. It only requires two controllable power components (IGBT or MOSFET) and two diodes. This topology is preferred for its ease of use and practicality in AMB applications. it is considered the most mature and suitable option for AMB's differential control. In AMBs, the coil currents responsible for controlling one Degree of Freedom (DOF) of motion are typically equal to the bias current, with the addition or subtraction of the control current. The coil current primarily undergoes changes near the bias current. Given these characteristics, the unidirectional current supplied by the half-bridge SPA proves to be sufficient for AMBs.

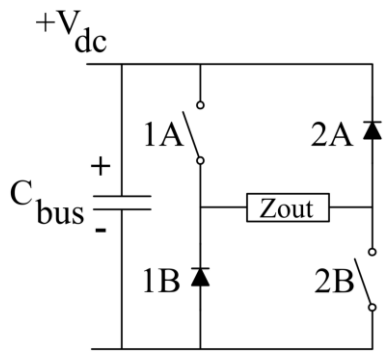

Figure 2 Half bridge topology.

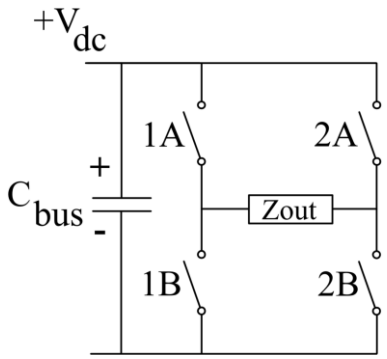

Figure 3 Full bridge topology.

However, it is important to note that the asymmetric half-bridge converter has two potential drawbacks when the design criteria prioritize overall efficiency and dynamic performance of the system. In such cases, the full bridge topology (Figure 3) may be worth considering for two reasons.

Firstly, it allows for the minimization of losses by employing MOSFETs (Figure 4) instead of diodes, resulting in improved efficiency.

Secondly, the full bridge configuration enables the injection of a negative current, which can enhance the dynamic behavior of the magnetic bearing, especially in the presence of eddy currents. In the following paragrah, a comparison will be made between a Si IGBT half-bridge SPA and a SiC MOSFET full-bridge SPA, exploring their respective characteristics and performance in AMB applications for $V_{dc} = 300\ V$ and $i_{amp} = 30\ A$.

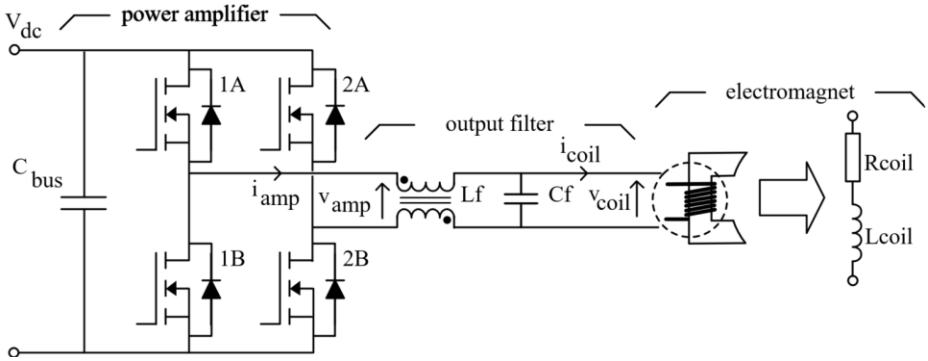

Figure 4 Full bridge SPA supplying one coil of the AMB actuator.

2.2. Integration

Figure 5 shows a visual comparison between Si and SiC SPAs and Figure 6 exhibits the SiC-SPA currently in qualification process. In the following, this paper brings performances on its design. The benefits of SiC are listed:

i) load Frequency: 8x faster.

ii) power Losses: 50 % lesser.

iii) heatSink volume: minimized.

iv) output cabinet filter: integrated within SiC-SPA.

v) system footprint: 65 % saved space.

vi) weight: 48.5 % lighter.

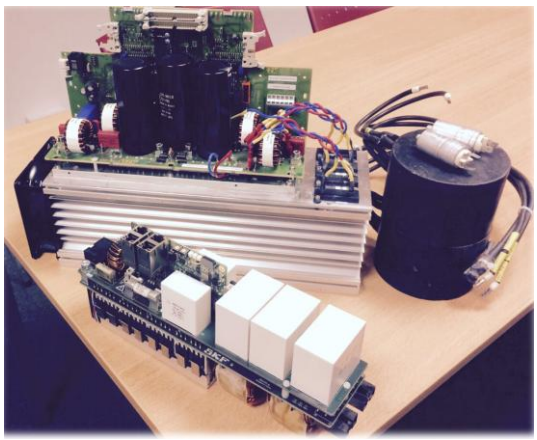

Figure 5 Layout Si (top) vs SiC (bottom).

Figure 6 SiC SPA: currently in qualification process.

2.3. Losses

As observed in previous publications, it is not surprising that the losses are lower in SiC-based configurations compared to those in Si-based configurations (Figure 7). This trend holds even when the switching frequency is multiplied by a factor of 10 or 14. The SiC version of the SPA consistently exhibits lower losses. Additionally, increasing the switching frequency has the added benefit of reducing the output filter of the SiC-based device, while maintaining low losses, as compared to the Si-based version of the device.

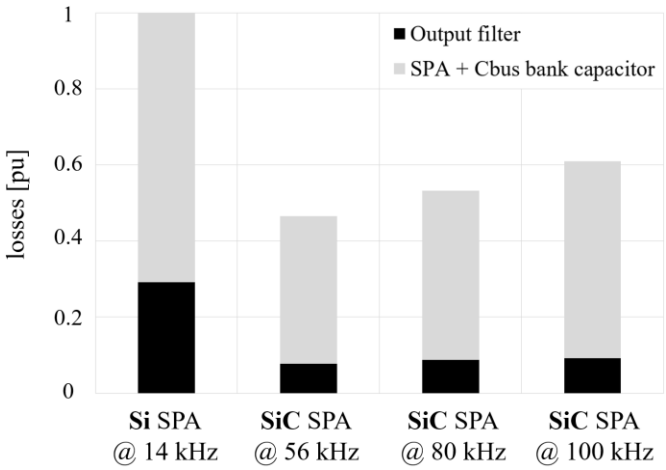

Figure 7 Comparison of losses between Si and SiC configuration..

2.4. Switching Mode

The IMPA operates in 3-level PWM method (cf. Figure 8). Benefiting from the increase of the switching frequency f_{sw} (SiC technology) the output load frequency f_{ap} is twice that applied to the command of each SiC-MOSFET ($f_{ap} = 2/T_{sw}$). This is a double impact: bandwidth increase and filtering optimization. The current ripple in the load and the voltage ripple in the capacitor bank terminals are reduced. Figure 9 shows the operation in the first quadrant. In STEPS 1 and 3 the energy is transferred from the capacitor $\boldsymbol{C_{bus}}$ to the bearing. Figure 10 shows the operation in the fourth quadrant. In STEPS 1 and 3 energy flows from the bearing to the capacitor $\boldsymbol{C_{bus}}$. STEPS 2 and 4: freewheeling steps.

When operating with any constant current, the duty cycle $D \approx 0.5$. The ripple Δi_{amp} tends to zero. The Table 1 illustrates some of the equations impacting the design.

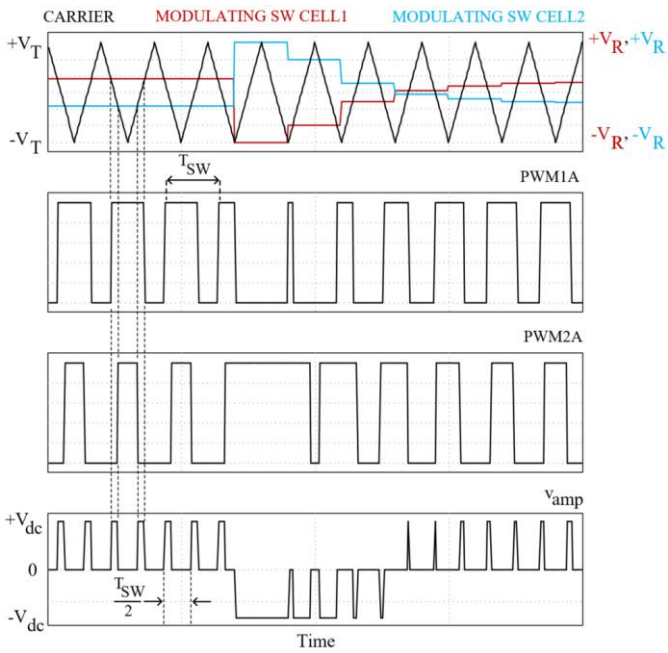

Figure 8 3-level PWM waveforms.

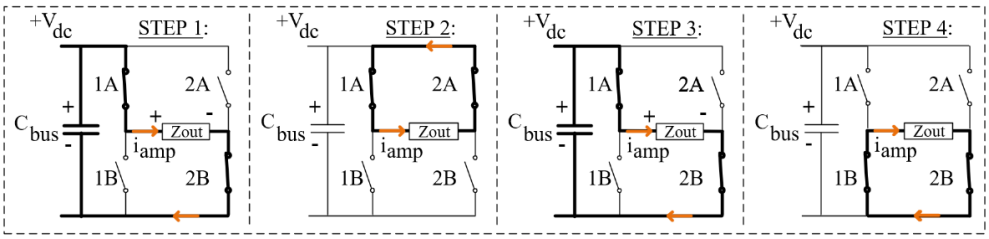

Command profile:

1A			1B	1A
2B	2A	2B		

Figure 9 Switching sequency in steady state configuration for $i_{coil} > 0$ and 2-levels v_{amp} ϵ [0, +V_{dc}].

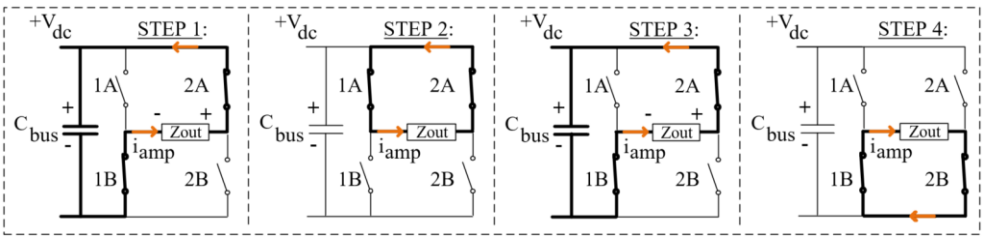

Command profile:

2A			2B	2A
1B	1A	1B		

Figure 10 Switching sequency in steady state configuration for $i_{coil} > 0$ and 2-levels v_{amp} ϵ [0, -V_{dc}].

Table 1 Summary of 3-level PWM method equations

Duty cycle for leg 1:	Duty cycle for leg 2:	Modulation index:
$D_1(t) = 0.5\,[m\,sin(\omega t) + 1]$	$D_2(t) = 0.5\,[m\,sin(\omega t - \pi) + 1]$	$m = V_R/V_T$
Duty cycle cases:		
$0 \le D \le 1/2$	$1/2 \le D \le 1$	$D = 1/4$ *or* $D = 3/4$
i_{amp} current ripple:		
$\Delta i_{amp} = \frac{V_{dc}}{L_f f_{sw}}(1-2D)D$	$\Delta i_{amp} = \frac{V_{dc}}{L_f f_{sw}}(2D-1)(1-D)$	$\Delta i_{amp}^{MAX} = \frac{1}{8}\frac{V_{dc}}{L_f f_{sw}}$
v_{coil} volage ripple:		
$\Delta v_{coil} \approx \frac{1}{4}\frac{V_{dc}}{L_f C_f f_{ap}^2}(2D-1)D$	$\Delta v_{coil} \approx \frac{1}{4}\frac{V_{dc}}{L_f C_f f_{ap}^2}(2D-1)(1-D)$	$\Delta v_{coil}^{MAX} \approx \frac{1}{32}\frac{V_{dc}}{L_f C_f f_{ap}^2}$

2.5. Passive Components

2.5.1. DC-link film Capacitor Bank C_{bus}

The dc bus capacitor needs to deal with the i) ripple current due to power amplifiers switching; ii) voltage fluctuation due to the source lead inductance; iii) voltage transient due to leakage inductance and SiC power device switching and iv) overvoltage due to regeneration the energy stored in the electromagnetics to the C_{bus} capacitor.

Inside the cabinet, all power amplifiers are connected to the fixed and non-regenerative common DC bus. In practice, the case (iv) is the most restrictive event. Improving the reliability, film technology is very suitable. Looking a trade-off between high RMS current values and reducing PCB (printed circuit board) footprint, the criterion considers the highest capacitive density per pcb area. For this, references from different manufactures (Kemet, TDK, Vishay, etc.) with different shapes could be evaluated. Figure 11 and Figure 12 show some examples.

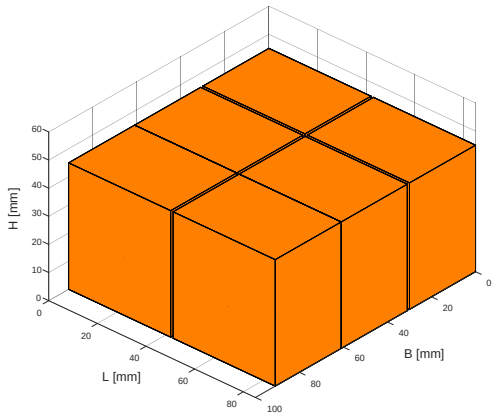

Figure 11 quantity = 6; total density: 5.6 µF/cm².

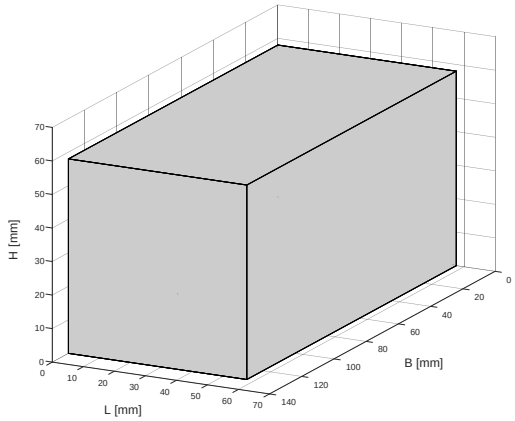

Figure 12 quantity = 1; total density: 6.4 µF/cm².

2.5.2. Output filter

In differential mode, many roles are assigned to this function (protecting the coil against the high dV/dt from the SiC, master the output HF current ripple reducing the cable losses, symmetrize the switching nodes at the output of the power amplifier. Different parameters are involved: i) power inductor ripple current; ii) output capacitor voltage ripple; iii) switching frequency value; iv) cutoff frequency; and v) mechanical volume for integration.

2.5.2.1. Output capacitor C_f

Figure 13 shows the relationship between C_f and its voltage ripple ΔVC_f and the output load frequency f_{ap}. A constant ripple current on the power inductor is considered and fully absorbed by the capacitor. For this analysis, due to SiC power device, the frequency range is large and the cutoff frequency cf. (1).

It is interesting to note that the largest C_f variation occurs in the first tens of kilohertz.

$$f_{cutoff} = \frac{1}{2\pi\sqrt{L_f C_f}} < \frac{f_{ap}}{2} \quad (1)$$

For the design, meeting the balance between power amplifier losses, thermal and EMC (dV/dt increase) behavior, and the compactness of passive elements, a trade-off to be kept in mind.

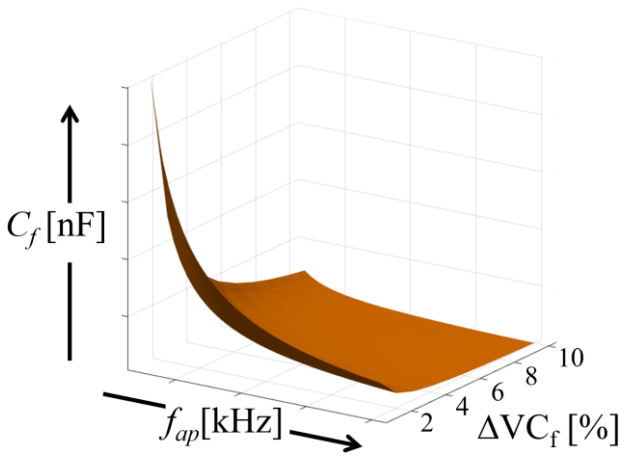

Figure 13 Output capacitor dependency.

2.5.2.2. Output Power Inductor L_f

The power inductor must handle a specified DC current within the electromagnetic actuator. Looking for the compactness, the design integrates the benefits of SiC-MOSFETs high switching frequency. Regarding the 3-level PWM modulation, two benefits integrate the design: i) frequency of the current ripple is increased twice: $f_{ap} = 2\, f_{sw}$; ii) current ripple amplitude minimized: $\Delta i_{amp}^{D=1/2} \approx 0$ (in steady state the required output voltage for the magnet is low: $D \approx 1/2$).

The approach to design considers the equation (2). The peak inductive energy storage (left side) cannot exceed the maximum magnetic energy storage capability of the core material (right side).

$$\frac{1}{2}L_f\left(i_{amp}^{peak}\right)^2 = \frac{1}{2\mu}(B_{core}^{MAX})^2 v_{core}^{MIN} \quad (2)$$

v_{core}^{MIN} is the minimum core volume and $B_{core}^{MAX} < B_{SAT}$ (magnetic non-saturation condition). This criterion (2) impacts the choice of the magnetic powder core: the v_{core}^{MIN} is proportional to the permeability. A toroidal core geometry and single-layer wound (better to heat extraction at high temperatures) are considered. Figure 14 shows the industrial packaging integrating both inductors: L_{Hf} and L_{Lf}.

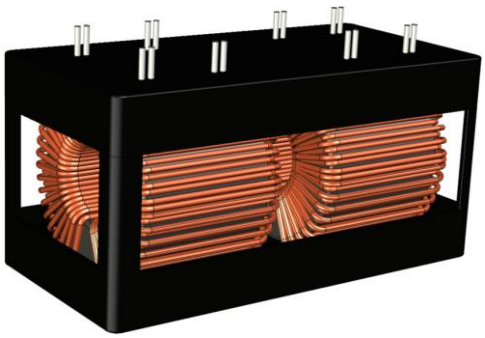

Figure 14 Industrial manufacturing packaging.

2.6. EMC Input Filter

For industrial applications, electromagnetic constraints are concerned, and requirements are set in a regulatory context. The switching power amplifiers generate significant electromagnetic conducted (EMC) interference in a broad spectrum and special attention must be considered related to the high switching frequency and fast time transitions of voltages and currents using SiC-MOSFETs. To minimize the global effort during the qualification of the whole active magnetic system, the approach to design is suppressed the disturbances per axis to an acceptable level.

Figure 15 shows (V_S: input voltage supply) a simplified EMC input filter structure and Figure 16 an equivalent common mode (CM) circuit. In common mode, the attenuation is achieved by the effect of the choke L_{MC} and the two C_Y capacitors. In differential mode (DM), the attenuation is carried out by the C_X and the dispersion inductance on L_{MC}.

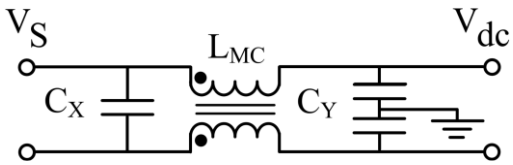

Figure 15 EMC Input filter topology.

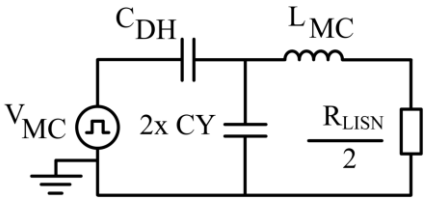

Figure 16 CM equivalent circuit (C_{DH}: parasitic capacitance).

For EMC tests for measurements, Figure 17 and Figure 18 summarize the equivalent circuits setup using the line impedance stabilization network (LISN).

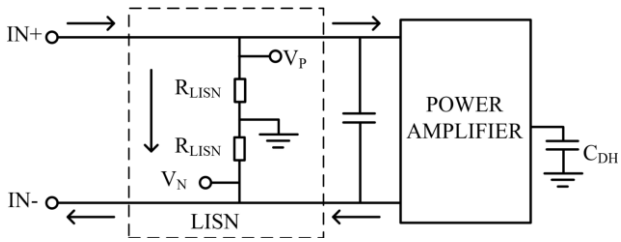

Figure 17 Equivalent circuit for differential mode conduction.

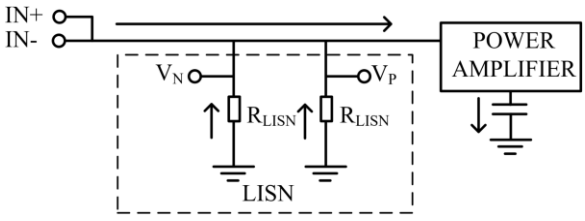

Figure 18 Equivalent circuit for common mode conduction.

L_{MC}, C_X and C_Y values result from an experimental and simulation approach. The EMC signature pf the power amplifier performing from 150 kHz to 30 MHz according to the IEC 61000-6-4.

2.7. Long cables influence

Figure 19 shows a simplified grounding diagram with a shielded cable. In the field, the cable length can reach up to 700 meters! R_C(resistance), L_C (inductance), C_P (capacitance) and G_P (conductance), are the parameters modeling the cable. Each parameter is a frequency-dependent function.

In addition to EMC impact, two potential issues are identified when connecting the magnetic bearings to a power amplifier with long cables: overvoltage and leakage currents. For predict and mitigate these different issues, a model with a series of elementary cells and (n+1) conductors is shown in Figure 20.

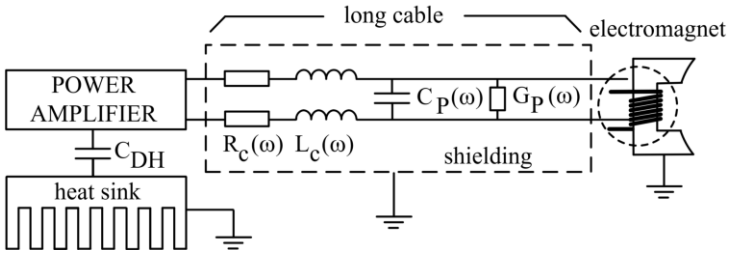

Figure 19 Simplified grounding diagram.

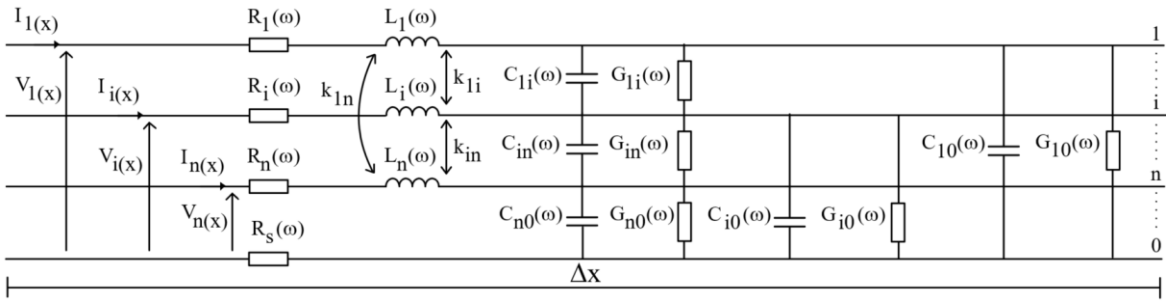

Figure 20 Elementary cell of multiconductor transmission

Based on the MTL (Multiconductor Transmission Line) theory, the cable can be modeled with a series of elementary cells. The work in [24] presents a practical solution for power cable characterization with the impedance analyzer. A cable with 12 conductors from Nexans is considered and the frequency band from 10 kHz to 30 MHz.

A proposal of a specific adapter, with spring connections, allows the power cables characterization for electromagnetic simulation. Considering the cable geometry and the uncertainty of measurement, with 76 impedance measurements, the development provides a protocol extracting the cable parameters in function of the frequency.

3. Environmental testing of the SiC Switching Power Amplifier

It is crucial to rigorously evaluate the reliability of SiC under extreme environmental conditions. Robust testing under challenging conditions is essential to ascertain the true performance and durability of SiC.

SiC-SPA qualification is currently in progress. In this chapter some qualification tests are presented. To carry out environmental tests, established standards set by the International Electrotechnical Commission (IEC) and the American Petroleum Institute (API) are considered: i) API-17F for thermal and vibration testing; ii) IEC 61000-6-4 for measurement of conducted disturbance and radiated field.

3.1. Thermal tests

Thermal testing is a crucial process used to assess the thermal fatigue resistance of solder joints, interconnections, and top contacts in electronic devices. Inside the climate chamber, this testing involves subjecting the Device Under Test (DUT) to hot and cold temperatures, while monitoring its performance during and after the test. After completion, an external visual inspection of the marking is also performed. Figure 21 and Figure 22 show the profiles carried out.

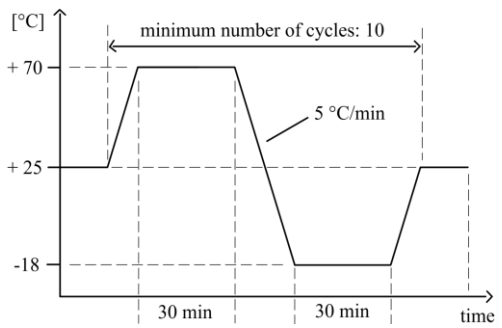

Figure 21 Cycling testing profile.

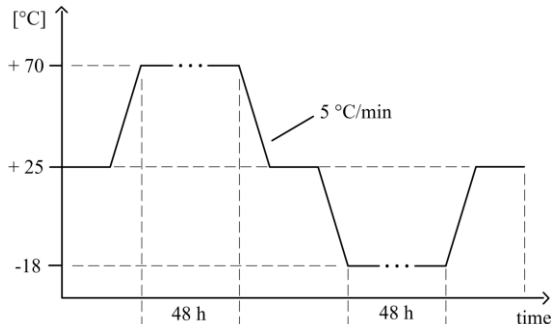

Figure 22 Soaking testing profile.

Several thermocouples are located inside (glued on the different electronic boards) and outside the casing. To evaluate the safety margin, Figure 23 summarizes it for 50 different electronic components. This is the difference between the maximum values from each manufacturer (extracted from datasheets) and the maximum temperature measured during the tests when the power amplifier delivers 100 % of its capacity (full load in operating point).

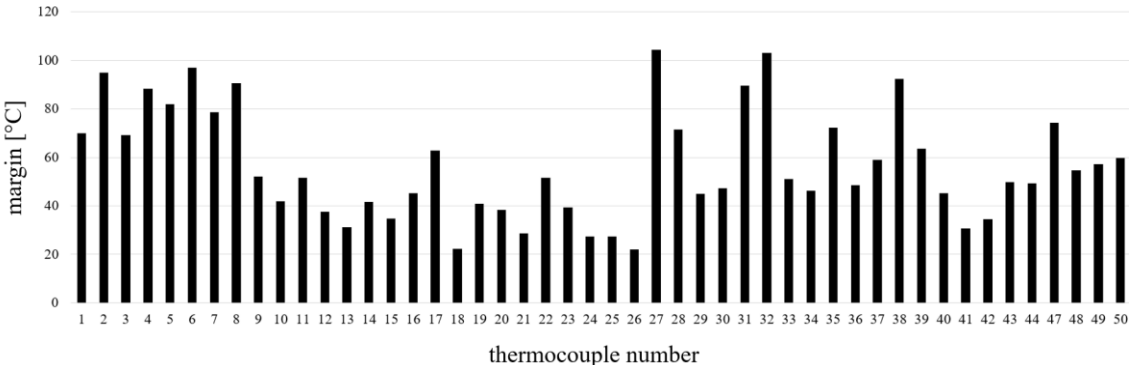

Figure 23 Temperature margins for 50 components equipped by thermocouples.

3.2. EMC/EMI

Figure 24 shows the measurement of conducted emissions generated by SPA. It the figure compares the signature without filtering to the solution with EMC filtering and improvement of the earth connections to the casing. In view of the standard (frequency $\in [150\ kHz;\ 30\ MHz]$) it is interesting to notice the net improvement impact.

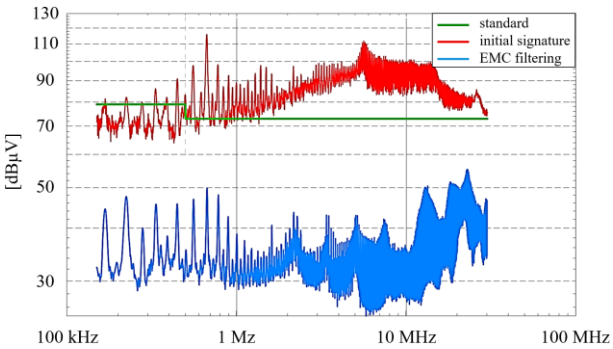

Figure 24 Measurement of conducted emissions.

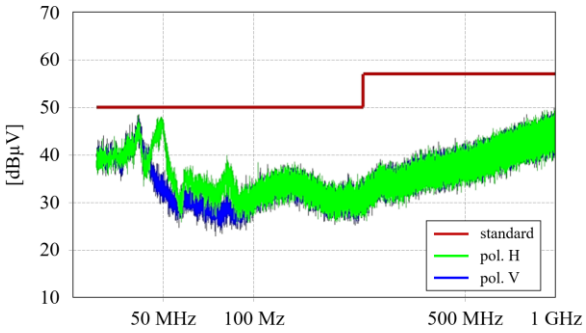

Figure 25 Measurement of radiated field.

Figure 25 shows the measurement of radiated emissions generated by SPA, results obtained inside an anechoic chamber. The horizontal (pol. H) and vertical (pol. V) polarized plans of oscillation were catch up. According to the standard (frequency $\in [30\ MHz;\ 1\ GHz]$) the results are very satisfactory.

Through careful design modifications and improvements, the measured results demonstrate unequivocal compliance with the standard, with emissions levels below the specified limits.

3.3. Vibration

During vibration and shock testing, it's important to ensure that the testing surface, such as the table surface, remains flat to accurately transmit the vibrations from the shaker to the DUT. The DUT is fastened to the platform (Figure 27). The SPA shall be undertaken with the DUT powered and with continuous monitoring of functions.

Before manufacturing the casing for the SPA, a finite element model predicting the mechanical modes was developed (Figure 26). The vibration test is a confirmation of the concept carried out for this design.

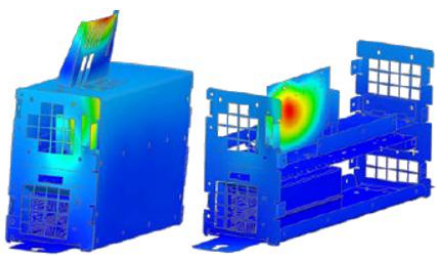

Figure 26 Modeling of mechanical modes.

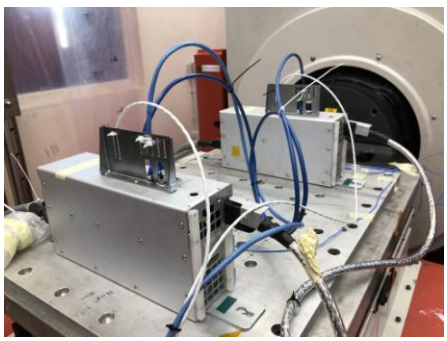

Figure 27 Assembly on vibration machine.

3.3.1. Sine sweep fatigue analysis

Test to find resonant frequencies that can excite the natural frequencies of the DUT. Test profile:

Table 2 Sine sweep profile

Parameter	*Value*
sweep rate	1 oct/min
frequency band	5 – 1000 Hz
number of sweeps	2 (1 up + 1 down)
level	5 – 25 Hz: 2 mm 25 – 1000 5 g

Figure 28 shows the experimental results for Y-axis. Each signature corresponds an accelerometer placed for acceleration measurement inside the DUT.

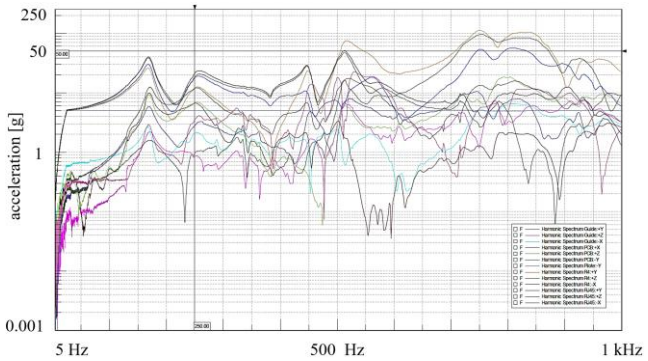

Figure 28 Frequency research following Y axis.

3.3.2. Shock test

Test to assesses the ability to survive a transient event by running a sharp transfer of energy. Test profile:

Table 3 Shock profile

Amplitude	*Duration*	*Number of shocks*	*Duration between pulses*
30 g	11 ms	4 positives and 4 negatives	1 s

Figure 29 shows the experimental results for Y-axis.

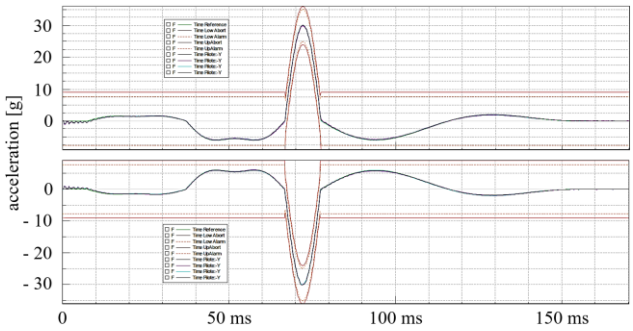

Figure 29 Driving curves during shock tests following the Y axis.

3.3.3. Random vibration fatigue

This test includes all the forcing frequencies which a shaker vibrates and excites all DUT resonances. Test profile:

Table 4 Random profile

Frequency [Hz]	*Slope [dB/octave]*	*Amplitude [g^2/Hz]*
20 – 80	+ 3	-
80 – 350	-	0.04
350 – 2000	- 3	-
RMS	-	6

Figure 30 shows the experimental results for Y-axis.

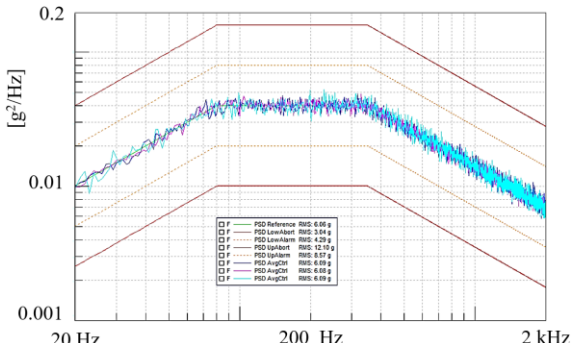

Figure 30 Driving curves during random following Y axis.

The experimental tests showed the robustness behavior regard to all profiles: no risk of plastification identified.

4. Conclusion

The SiC SPA has been analyzed and compared to the Si SPA, revealing its potential as a more efficient and lightweight solution with reduced losses even at very high switching frequency. Moreover, the SiC SPA has undergone several environmental cycling tests and has successfully met IEC and API standards. However, further qualification tests need to be conducted to ensure its reliability and durability under more demanding conditions, such as when mounted on a cabinet subject to vibrations, shocks, and EMC.

Overall, the SiC SPA is a promising technology that offers significant advantages over traditional Si SPAs and has the potential to become a valuable solution for a wide range of applications.

References

[1] A. Elasser, T.P. Chow, "Silicon Carbide Benefits and Advantages for Power Electronics Circuits and Systems". IEEE proc, Vol. 90, pp. 969-986, 2002, [CrossRef]

[2] J. Bielaall, et all, "SiC vs. Si-Evaluation of potentials for performance improvement of Inverter and DC-DC Converter Systems by SiC Power Semiconductors", IEEE Trans. on Industrial Electronics, Vol. 58, No. 7, July 2011, [CrossRef]

[3] J. Millán, et all, "A Survey of Wide Band Gap Power Semiconductor Devices," IEEE Trans. on Power Electronics., Vol. 29, No. 5, pp. 2155-2163, May 2014, [CrossRef]

[4] T. Neyer, "What's the difference between Silicon Carbide and Silicon", website electronicdesign.com, March 2, 2022, [CrossRef]

[5] S. Daryanani, "The road to 200-mm SiC Production", Website Power Electonic news, June 14, 2022, [CrossRef]

[6] M. Di Paolo Emilio, "SiC Power Devices: Lowering costs to Drive Adoption", Website Power Electonic news, January 18,2022, [CrossRef]

[7] W. Cai, et all, " Review and Development of Electric Motor Systems and Electric Powertrains for New Energy Vehicles", Automotive innovation , vol 4, Feb 2021, [CrossRef]

[8] STmicroelectronic, " E-mobility SiC Traction Inverter", APEC 2020, March 2020, [CrossRef]

[9] M. Nitzsche, et all, " Comprehensive comparison of a SiC MOSFET and Si IGBT based Inverter", PCIM 2019, May 2019, [CrossRef]

[10] E. Ayerbe, J.Shao, "SiC Mosfet Based Bi-Directional 3 phase AC/DC converter", internal presentation CREE 2017

[11] P. W. Wheeler, "The more electric aircraft: Why aerospace needs power electronics?" Power Electronics and Applications, 2009. EPE '09. 13th European Conference on, pp. 1-30, Sept. 2009, [CrossRef]

[12] A.J. Wileman, et all, "A roadmap for reliable power electronics for more electric aircraft", Progress in Aerospace Sciences, Vol 127, Nov 2021, [CrossRef]

[13] B.J. Nel, S. Perinpanayagam, " A brief overview of SiC MOSFET failure modes and design reliability", 5th Int Conf TesConf 2016, [CrossRef]

[14] C. Chen, et all, " Study of Short-circuit Robustness of SiC MOSFETs, analysis of the failure modes and comparison with BJTs", Microelectronics Reliability,Vol 55, pp 1708-1713, August 2015, [CrossRef]

[15] A. Castellazzi , et all, "Sic Power MOSFETs performance, robustness and technology maturity", Microelectronics reliability Vol 58, pp 164-176, March 2016, [CrossRef]

[16] S. Jagdale, "Reliability and robustness tests for Next-generation high voltage SiC Mosfets", Power electronic news, June 2022, [CrossRef]

[17] S. Daryanani, "The SiC MOSFET reliability studies at the Ohio State University: Threshold Voltage Stability and Gate Oxide Screening Challenges", Power electronic news, Sept 2022, [CrossRef]

[18] M. Furukawa, et all, " Improved reliability of 1.2 kV SiC MOSFET by preventing the intrinsic body diode operation", PCIM 2020, [CrossRef]

[19] L. C. Yu, et all, "Reliability issues of SiC MOSFETs: A technology for high temperature Environments", IEEE Trans. on Device and Materials Reliability, Vol.10, NO.4, pp 418-426, Dec 2010, [CrossRef]

[20] Y.Xu, et all, " Experimental assessment of high frequency bearing currents in an induction motor driven by a SiC Inverter", IEEE Access, vol 9, pp 40540-40549, March 2021, [CrossRef]

[21] D. Aggeler, J. Biela, J.W. Kolar, "Controllable dV/dt behavior of the SiC MOSFET/JFET Cascode, an alternative hard commutated Switch for telecom applications", APEC 25th conference, Feb 2010, [CrossRef]

[22] S. Hazra, et all, "High switching performance of 1700V, 50A SiC power MOSFET over Si IGBT/BiMOSFET for advanced power conversion applications", IEEE transaction on power electronics, Vol. 31, Issue 7, pp 4742-4754, July 2016, [CrossRef]

[23] M. di Benedetto, et all, "Efficiency Comparison of 2-level SiC inverter and soft switching Snubber SiC inverter for electric motor drives", Energies 2021, Vol .14, issue 16, pp 1-17, 2021, [CrossRef]

[24] T. G. Bade, J. Roudet, A. Derbey, A. de Andrade, L. Sadi-Haddad, "Adapter for the Impedance Measurement of Power Cable with an Impedance Analyzer" IEEE Transactions on Electromagnetic Compatibility, 14 March 2023 [CrossRef]